INTERSTELLAR DUST PROPERTIES OF M51 FROM *AKARI* MID-INFRARED IMAGES

FUMI EGUSA[1], TAKEHIKO WADA[1], ITSUKI SAKON[2], TAKASHI ONAKA[2], KO ARIMATSU[1,2], AND HIDEO MATSUHARA[1]

[1] Institute of Space and Astronautical Science, Japan Aerospace Exploration Agency, Sagamihara, Kanagawa 252-5210, Japan; fegusa@ir.isas.jaxa.jp
[2] Graduate School of Science, The University of Tokyo, Bunkyo-ku, Tokyo 113-0033, Japan

ABSTRACT

Using mid-infrared (MIR) images of four photometric bands of the Infrared Camera on board the *AKARI* satellite, S7 (7 μm), S11 (11 μm), L15 (15 μm), and L24 (24 μm), we investigate the interstellar dust properties of the nearby pair of galaxies M51 with respect to their spiral arm structure. The arm and interarm regions are defined based on a spatially filtered stellar component model image and we measure the arm/interarm contrast for each band. The contrast is lowest in the S11 image, which we interpret as meaning that among the four *AKARI* MIR bands, the S11 image best correlates with the spatial distribution of dust grains including colder components. On the other hand, the L24 image, with the highest contrast, traces warmer dust heated by star forming activity. The surface brightness ratio between the bands, i.e., color, is measured over the disk of the main galaxy, M51a, at 300 pc resolution. We find that the distribution of S7/S11 is smooth and traces the global spiral arm pattern well while L15/S11 and L24/S11 peak at individual H II regions. This result indicates that the ionization state of polycyclic aromatic hydrocarbons (PAHs) is related to the spiral structure. Comparison with observational data and dust models also supports the importance of the variation in the PAH ionization state within the M51a disk. However, the mechanism driving this variation is not yet clear from the currently available datasets. Another suggestion from the comparison with the models is that the PAH fraction in the total dust mass is higher than previously estimated.

Key words: dust, extinction – galaxies: individual (M51) – galaxies: spiral

Online-only material: color figures

1. INTRODUCTION

Interstellar dust is abundant and widely distributed, particularly within the disks of late type galaxies. Since the properties of dust reflect conditions of its environment, emission from dust is an important probe of the interstellar medium (ISM). Dust around star-forming regions absorbs intense star light and radiates the absorbed energy in the infrared (IR) regime. Given this close connection between IR emission and the UV–optical extinction, the 24 μm band flux has recently been used to correct for the extinction effect on the star formation rate derived from optical Hα emission (Calzetti et al. 2007). At shorter wavelengths, many spectral band features are observed and polycyclic aromatic hydrocarbons (PAHs) have been thought to be their major carriers (e.g., Leger & Puget 1984; Sellgren 1984; Allamandola et al. 1989; Draine 2003; Tielens 2008). These features at different wavelengths are thought to represent PAHs in different conditions (Draine & Li 2007). For example, the 7.7 μm feature, which is bright in star forming sites, mostly originates from ionized PAHs, while neutral and ionized PAHs equally contribute to the 11.3 μm feature. Features at shorter wavelengths are generally emitted from smaller grains and vice versa. Ratios of these PAH band features are thus used to investigate the environment and properties such as temperature and ionization state (e.g., Galliano et al. 2008; Mori et al. 2012).

M51 is a pair of galaxies which are a grand-design spiral galaxy, M51a (NGC 5194), and a companion galaxy, M51b (NGC 5195). Given its proximity and prominent two-armed spiral structure, M51 has been a popular target for ISM and spiral arm pattern studies. From optical and UV images, properties of H II regions and star clusters over the entire disk of M51a have been investigated and their ages in the arms have been found to be younger than those in the interarm area (Lee et al. 2011; Sánchez-Gil et al. 2011). Their natal clouds are traced by radio CO lines and the largest clouds, which are thought to be progenitors of massive star clusters, are only found in

the arms (Koda et al. 2009). These results indicate that star formation dominantly occurs in spiral arms. Egusa et al. (2011) investigated the evolutionary sequence of molecular gas *within* an arm using very high angular resolution CO data and found that cloud cores, which eventually form stars, are formed through the passage of spiral structure. On the other hand, studies of warm and hot interstellar dust components with mid-IR (MIR) observations are rather limited. For selected locations, Sauvage et al. (1996) analyzed 7 μm (LW2) and 15 μm (LW3) images of M51 from the *Infrared Space Observatory (ISO)*/ISOCAM and found that LW2/LW3 becomes small in the spiral arms, which they attribute to a temperature variation. From the MIR spectra toward a central $\sim$3$'$ × 3$'$ area of M51a, Galliano et al. (2008) derived the PAH band ratio of 7.7 μm/11.3 μm to be higher in the spiral arms. These results indicate warm and ionized dust in spiral arms but the variation of dust properties across the entire disk has not yet been investigated.

The Infrared Camera (IRC; Onaka et al. 2007b) on board the *AKARI* satellite (Murakami et al. 2007) has the advantage of a wide field of view (FoV) of $\sim$10$'$, comparable with the size of the whole M51 system. In addition, three channels, near-IR (NIR), MIR-S, and MIR-L, and three bands in each channel cover the wavelength range of 2–25 μm *continuously*. In Figure 1, the relative response curves of the MIR bands used in this study (S7 and S11 for MIR-S and L15 and L24 for MIR-L, while the numbers after S or L denote the representative wavelength in μm) are plotted together with template spectra for neutral PAHs, ionized PAHs, and dust grains with $T = 100$ K. PAH spectra are from Draine & Li (2007) provided by DustEM (Compiègne et al. 2011) and the modified blackbody spectrum is used to represent the $T = 100$ K dust component. These spectra are also used in this study and fully described in Section 4.3. As illustrated in the figure, *AKARI* MIR bands efficiently trace the interstellar dust in different conditions, helping to clearly reveal the dust properties. The angular resolution, i.e., the FWHM of a point-spread function (PSF), is 4$''$.0–6$''$.8,
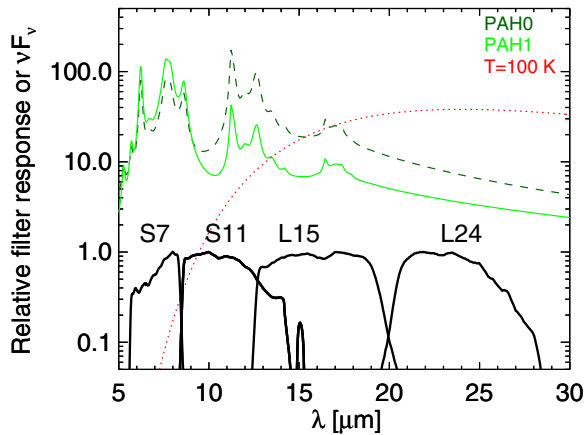
Figure 1. Relative MIR filter response curves normalized to a peak of unity (thick solid black lines), together with spectra for neutral PAHs (PAH0; dashed dark green), ionized PAHs (PAH1; solid light green), and a modified blackbody with $T = 100$ K (dotted red).

(A color version of this figure is available in the online journal.)

Table 1
Parameters of M51a

Parameter	Value	Reference
R.A. (J2000)	13:29:52.711	NED
Decl. (J2000)	+47:11:42.62	NED
P.A. (deg)	169.0 ± 4.2	Daigle et al. (2006)
Inc (deg)	24 ± 3	Shetty et al. (2007)
Distance (Mpc)	8.4	Feldmeier et al. (1997)

Note. The NASA Extragalactic Database (NED) centers, originally from radio continuum observations (Turner & Ho 1994), are $<1''$ from the dynamical centers derived by Shetty et al. (2007).

depending on the observing wavelength, and is high enough to investigate structures within the galactic disk. With these characteristics, *AKARI* images provide valuable information for understanding interstellar dust conditions and their relationship with environments such as star forming activity and galactic structures.

In this study, we use *AKARI* MIR images to understand the dust properties in M51 and investigate their spatial variation to determine to what extent the grand-design spiral structure has an effect. We find that the 11 μm image is of great importance for exploring PAH conditions such as ionization state and the PAH fraction compared with the total dust mass. The adopted parameters of M51a are listed in Table 1. At a distance of 8.4 Mpc, $1''$ corresponds to 41 pc.

2. DATA REDUCTION

2.1. IRC Data Sets

By design, NIR and MIR-S share the FoV while MIR-L is offset by $\sim 25'$. Each covers about $10' \times 10'$, which is almost the same size as the M51 system. Properties of the datasets used in this study are summarized in Table 2. They were taken as a part of the mission program, "ISM in our Galaxy and Nearby Galaxies" (ISMGN; Kaneda et al. 2009) and the astronomical observation template (AOT) 02 was used. In this AOT, two bands in each channel were used and one observing cycle is one short and one long exposures in the NIR and one short and three long exposures in the MIR. A slight position change (dithering) was performed every cycle to minimize the effect of unusable pixels due to hot pixels and cosmic rays.

Table 2
Properties of the M51 *AKARI*/IRC Datasets

ID	Obs Date	Filters	Short, Long
1400387.1	2006 Dec 16	N3, N4	4, 4
		S7, S11	4, 12
1402202.1	2007 Jun 16	L15	3, 9
		L24	4, 12

The datasets were retrieved through the Data ARchives and Transmission System (DARTS),[3] and raw images were processed with the latest IRC imaging toolkit, a package of the Image Reduction and Analysis Facility (IRAF)[4] scripts available via the *AKARI* observers page.[5]

In the following part of this section, we briefly describe the reduction procedures that are not included in the standard pipeline but are necessary for the M51 data. Detailed descriptions for some of these procedures are presented in a separate paper (F. Egusa et al. 2013, in preparation).

2.2. Neighbor Dark Frames

Since the observations in orbit started, the number of hot and warm pixels has increased with time, particularly in the MIR-L channel. The super dark frames were created from the datasets taken at the very early stage of the satellite operation and thus are not most suited to datasets taken at later stages. A few dark frames for each channel and exposure were taken at the beginning and the end of each pointed observation and the self dark frames are generally created from so-called pre-dark frames taken prior to the object frames. They are, however, less reliable due to the small number of frames combined.

We thus created a new set of dark frames called a neighbor dark. The concept is that combining dark frames taken in a certain period of time increases the number of data combined (relative to the self dark) and better calibrates the temporal variations (relative to the super dark).

2.3. Earth Shine Light Removal

The background of the MIR-L frames of M51 was found to be contaminated by earth shine light (EL). Since the EL pattern is extended, it is difficult to separate it from the object, M51. In addition, its amplitude varied significantly during the observations as the separation angle between the telescope and the earth changed. We have thus created an EL template for each MIR-L band from datasets taken under similar conditions (i.e., date and coordinates) and successfully removed the EL component from the MIR-L frames. Scripts for creating and removing the EL template are also included in the IRC toolkit.

In the case of M51, the maximum EL contamination was about 2 and 30 MJy sr^{-1} for L15 and L24, respectively. The former is comparable with the faint diffuse emission in the interarm regions, while the latter reaches a brightness of the H II regions in the spiral arms.

2.4. Stacking

For the sake of PSF correction, the pixel scale of MIR images was divided in half, i.e., one pixel was divided into 2×2 pixels, before stacking.

For MIR-L images, only a few stars were available within the FoV to calculate shifts between the frames. The reduction toolkit instead picked up objects in M51, mainly bright spots in spiral arms. In order to check the validity of shift values derived, we used the IRAF task xregister, which calculates a cross correlation between two images and determines relative shifts in the x- and y-directions. An area for calculating the cross correlation was carefully selected so as to exclude masked pixels. A script to perform this procedure is also included in the IRC toolkit as an alternative when the normal coadd process fails, particularly useful for diffuse objects observed in the MIR-L channel.

In the case of MIR images of M51, we confirmed that the shift values derived by the normal coadd and xregister are consistent to within 0.5 pixel. Only the frames with long exposure were stacked.

2.5. WCS Registration

For NIR images, the World Coordinate System (WCS) information was automatically set by the IRC toolkit, which uses the Two Micron All Sky Survey (2MASS) point source catalog. For MIR images, on the other hand, the number of stars in the FoV was not enough to derive the accurate coordinates for the toolkit. We thus picked up stars in the stacked image manually and obtained their coordinates in the USNO catalog with the help of the Aladin software. For the MIR-S images, about five stars were found to be useful, while only two stars were found in the FoV of the MIR-L images. As a consequence, we had to add the nucleus of M51a. Based on the position of these stars in the image plane and their coordinates, the WCS header parameters were derived and updated with the use of the IRAF task ccmap. In order to assess the validity of this procedure, we derived the coordinates of the N4 image and confirmed that they were consistent with the toolkit-derived coordinates. The rms of the coordinate fitting was $\sim$1″ for the NIR and MIR-S images and $\sim$2″ for the MIR-L images. With all the six images whose WCS information was set, we confirmed that their coordinates were consistent between the bands and also with other archival images.

2.6. PSF Correction

In order to discuss brightness ratios between different bands, we applied a PSF correction to the four MIR band images. The PSF template for each MIR band is provided by Arimatsu et al. (2011). The corrected PSF is two-dimensional Gaussian with FWHM of 7″.4, which is slightly larger than the original L24 PSF and corresponds to $\sim$300 pc at the distance of M51.

2.7. A Ghost in MIR-S

A bright compact object close to M51b in the southwest direction, which is apparent only in the S7 and S11 images, was found to be an artifact called a ghost of this companion galaxy, arising from internal reflection in the beam splitter. The peak flux of the ghost relative to M51b is larger in the S11 data. Arimatsu et al. (2011) examined major artifact features including the ghost in MIR images and provided their template patterns for each band.

We tried to remove this ghost component from the stacked S11 image before the PSF correction in two different ways. We first made a model ghost pattern from the flux distribution of the companion galaxy by convolving it with the ghost template. Since the model did not fit the observed pattern perfectly, we then tried to remove it by employing the CLEAN algorithm (Högbom 1974), which has been used for deconvolution of radio interferometer images. However, a CLEANed image showed a residual pattern, which could not be neglected.

We thus concluded that the ghost template is not applicable to the M51 S11 image. The reason is plausibly a combination of the following facts. First, the template is made for a bright source at the center of the FoV. A spatial pattern for an object around the edge, which is the case for M51b, can be different. In fact, the peak position of the observed ghost is slightly off from the expected position. Second, the ghost amplitude is known to depend on the source color (Arimatsu et al. 2011). Third, the count of the source, M51b, is very high and close to the saturation limit. For such a bright source, the uncertainty in the linearity correction would be rather large. The latter two facts can explain the failure in modeling the ghost, but not in the CLEANing.

We therefore decided to mask a circular area with a radius of 15″ around the observed ghost in the S11 image. The same area was also masked in the S7 image. The masking was performed after the PSF correction.

2.8. Regridding and Flux Calibration

The flux conversion factors provided by Tanabé et al. (2008) were applied to our datasets. The 1σ uncertainties of the conversion factors were estimated to be $\sim$2% for S7 and S11, $\sim$3% for L15, and $\sim$5% for L24. A color correction was not applied. We note here that a sky background was subtracted before flat fielding.

All images were aligned north up and east left and regridded to 3″.7 pixel^{-1} (Figure 2).

The surface brightness distribution at S7, L15, and L24 was compared with that of *Spitzer* IRAC4, *ISO* LW3, and *Spitzer* MIPS24, respectively. PSF matching was performed if necessary. We found that the corresponding two datasets are linear with a slope around unity.

3. ANALYSIS

3.1. Stellar Component Distribution

While dust is the dominant source of MIR emission in galaxies, the stellar contribution is sometimes non-negligible at shorter wavelengths and strongly depends on the total stellar mass, the star formation history, and so on. Mentuch Cooper et al. (2012) fit stellar spectral energy distributions (SEDs) generated by the PEGASE.2 code (Fioc & Rocca-Volmerange 1997) to optical and NIR images of M51 and derived a set of best-fit parameters of the stellar population for each pixel. Based on this model of stellar distribution, the contribution from stars in the *AKARI* MIR bands was calculated and subtracted from individual band images so that they represent dust-only properties. The stellar fraction of the total MIR flux was typically a few percent and higher values ($\sim$20%) were found in a part of the spiral arms at shorter wavelengths.

In addition to stars in M51, foreground Milky Way (MW) stars were visible in some *AKARI* images space. In order to identify such foreground stars, we performed aperture photometry on the S7 image of sources listed in the 2MASS point source catalog within the FoV and compared the S7 flux with the K magnitude. We manually set a border between foreground stars and extragalactic sources in the S7 – K plot and defined $\sim$20 sources as plausible foreground stars. Pixels within 7″.4 of these stars were masked out.
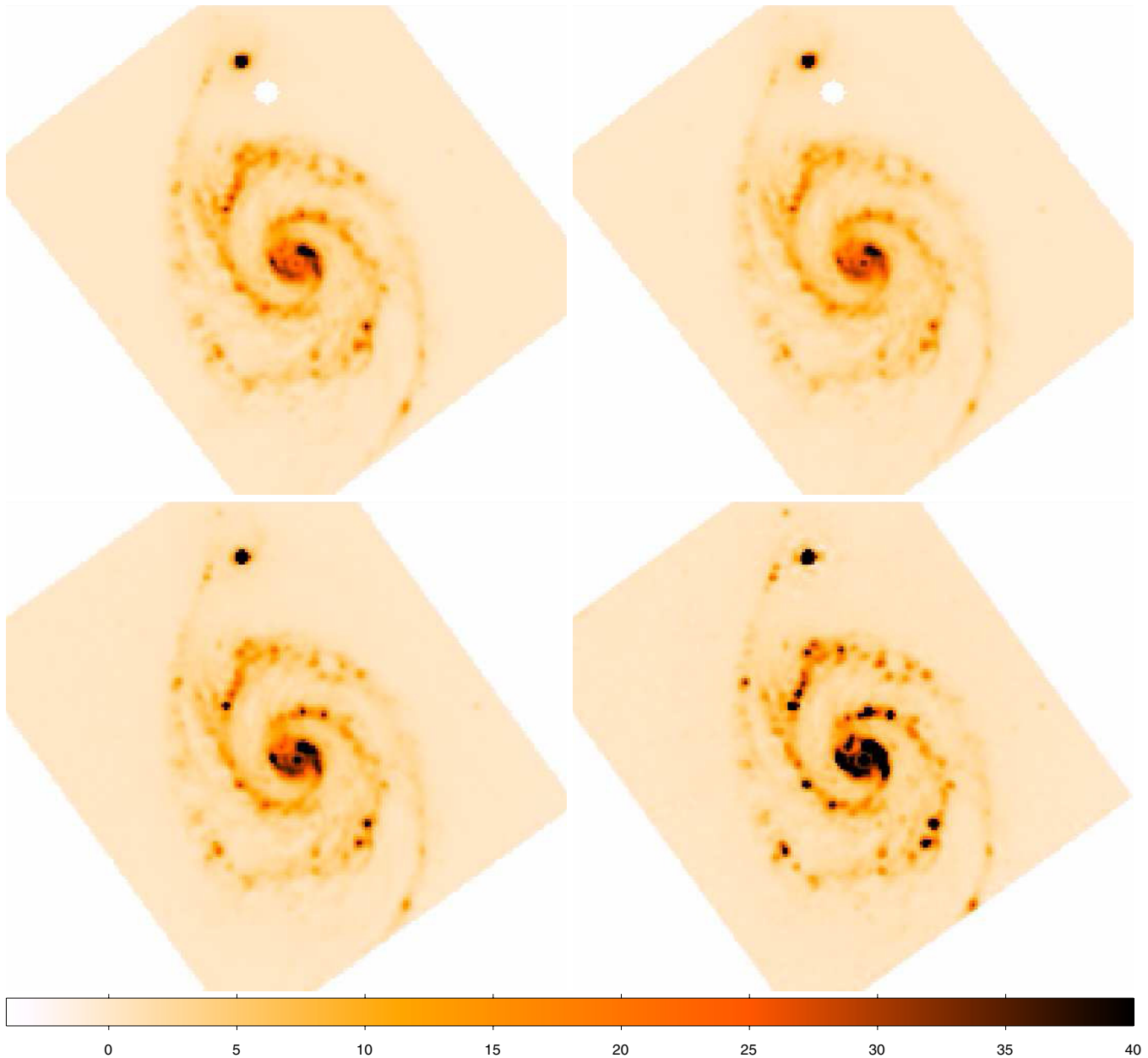
Figure 2. PSF corrected, aligned, and calibrated images for four MIR bands, S7 (top left), S11 (top right), L15 (bottom left), and L24 (bottom right). The FWHM of the corrected PSF is $7\rlap{.}''4$ and the pixel size is $3\rlap{.}''7$. The units for color scale are MJy sr^{-1}. The ghost has been masked in S7 and S11. The stellar contribution is not subtracted.

(A color version of this figure is available in the online journal.)

All the results and discussions presented in Sections 4 and 5 are based on the dust only images created from stellar subtraction and masking described in this subsection.

3.2. Arm/Interarm Definition

In this study, we basically followed the procedures of Dumas et al. (2011), who applied wavelet analysis to the 20 cm radio continuum image of M51 to separate arm and interarm regions. Since stars dominate the baryonic mass and thus the gravitational potential of the galactic disk, we used the model stellar distribution of Mentuch Cooper et al. (2012) discussed above to define the arm and interarm regions.

We first deprojected the image to obtain a face-on view of M51 with the disk orientation parameters listed in Table 1.

An azimuthal average was calculated at each radius and subtracted to remove axisymmetric components and thus enhance the asymmetric spiral arm structure. The central region with $r \leqslant 30''$ from M51a, the area within $80''$ from M51b, and the foreground stars defined in the previous subsection were masked out.

Following Dumas et al. (2011), we then applied wavelet analysis with Pet Hat function in order to extract a specific spatial scale. The result was consistent with Dumas et al. (2011); the scale of $83''$ (or 3.4 kpc) was suitable to delineate the two-armed spiral structure of the M51a disk. Our definition appears to be smoother than theirs since we used the stellar distribution, while they used the 20 cm image, which traces the synchrotron emission from supernova remnants and the diffuse ISM and thus is more sensitive to smaller structures.
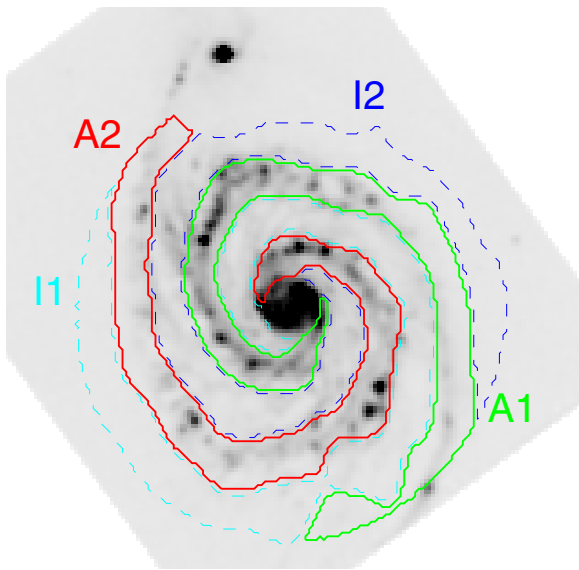
Figure 3. Arm and interarm definition of M51a. Areas enclosed by solid green and red lines are defined as arms (labeled A1 and A2), while those with cyan and blue dashed lines are interarm regions (labeled I1 and I2). The background is the L15 image.

(A color version of this figure is available in the online journal.)

Figure 4. Surface brightness histogram of each region for each band. Colors correspond to the arm definition shown in Figure 3 and black is for the central region. The vertical dashed line indicates 5σ of each band.

(A color version of this figure is available in the online journal.)

The minimum and maximum radii of the disk were set to be $30''$ and $240''$, respectively. The area within $80''$ from the companion was also excluded, as discussed above. We separated the disk into arm and interarm regions according to the sign of the wavelet component map with the $83''$ scale. Plus and minus correspond to arm and interarm, respectively. The area not connected to the central region was also excluded. Following Egusa et al. (2009), Arm 1 was defined as extending in the opposite direction to the companion, while Arm 2 was defined to be connected to the companion. This arm and interarm definition is shown in Figure 3. Pixels outside the defined area are excluded in the following.

4. RESULTS

4.1. Flux Distribution and Arm/Interarm Contrast

The four MIR images shown in Figure 2 are similar overall in the sense that they are bright in the center of the two galaxies and in the spiral arms of M51a. In Figure 4, the surface brightness histogram for each region defined in Section 3.2 and each *AKARI* MIR band is presented. The histogram for the central region is distinct with the largest peak value and the narrowest profile width. The histograms for the arm and interarm regions, on the other hand, show broader profiles with peaks around 1.0–10 MJy sr^{-1}. These broader profiles are likely due to the definition of the arms, which includes bright H II regions and fainter areas. The interarm filamentary structures, which are called feathers or spurs and are often as bright as the arm structures, may also play a role (See Section 4.2.1 for a discussion in more detail).

We have calculated the brightness ratio of arm to interarm regions, i.e., the arm/interarm contrast, at each $10''$ width annulus. It varies from 1 to 5, with higher values found where bright star forming regions belong to the arms. The mean values of the arm/interarm contrast are 2.9 for S7, 2.5 for S11, 2.7 for L15, and 3.1 for L24. The highest contrast for L24 indicates that it best traces the warm dust (WD) around star forming regions in
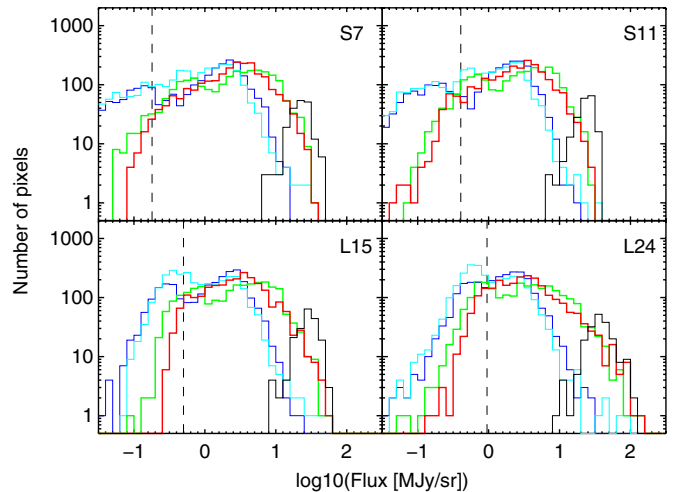
the arms. Although S7 is expected to trace star forming activity, its arm/interarm contrast is lower than that of L24 since S7 is also bright in the feathers. On the other hand, S11 exhibits the lowest contrast, implying that flux around 11 μm is less sensitive to environment. Consistently, Onaka et al. (2007a) found a constant *IRAS* 12 μm/far-IR (FIR) ratio over a wide range of temperatures. For elliptical galaxies where properties of dust grains and their heating sources can be different from those in spiral galaxies, Kaneda et al. (2007) found a good correlation between the equivalent width of the PAH 11 μm feature and the FIR/MIR ratio. These results suggest that the 11 μm brightness correlates well with the total amount of dust including colder components, which dominate the FIR flux. L15 seems to be a combination of S11 and L24, with a diffuse dust distribution similar to S11 and a few bright spots corresponding to the nuclei and brightest H II regions.

4.2. Color Distribution

A surface brightness ratio map between two bands (i.e., a color map) of M51 was created from two band images using all the pixels brighter than 5σ in both images. Colors based on S11, i.e., S7/S11, L15/S11, and L24/S11, are presented in Figure 5 with the defined arm and interarm regions. S11 was selected to be the denominator because it shows the lowest arm/interarm contrast and thus is thought to best represent the total dust distribution among the four *AKARI* MIR bands. Note that the signal-to-noise ratio of the color is lower at larger radii where it is close to the boundary. The high L15/S11 values at the east end may be artificial due to residuals of the EL subtraction. In addition, the L24/S11 color around M51b is erroneous due to residuals from the PSF correction.

In Figure 6, histograms of colors are presented for the defined regions. The difference between the regions are less distinct compared with the histograms of surface brightness (Figure 4).

In Figure 7, these colors are plotted against radius. The color averages are calculated within an annulus of $10''$ radial width and overplotted with lines color-coded in the same way as Figure 3. We find that they are mostly flat, indicating that the large dispersion seen in the histogram (Figure 6) is not due to a radial gradient of colors. Using *Spitzer* IRAC and MIPS photometric datasets, Muñoz-Mateos et al. (2009) constructed
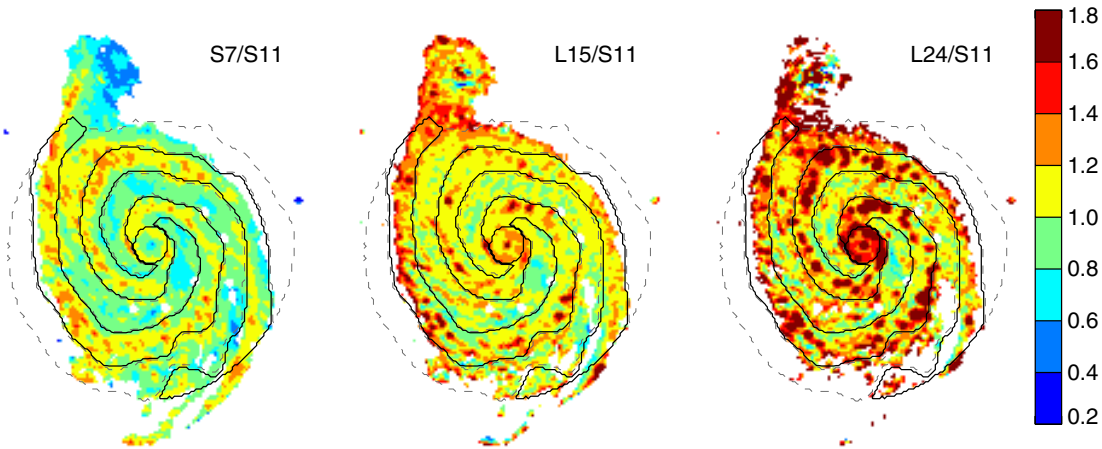
Figure 5. Map of colors: S7/S11 (left), L15/S11 (middle), L24/S11 (right). The arm and interarm regions defined in Section 3.2 are indicated by thick solid black and thin dashed gray lines, respectively.

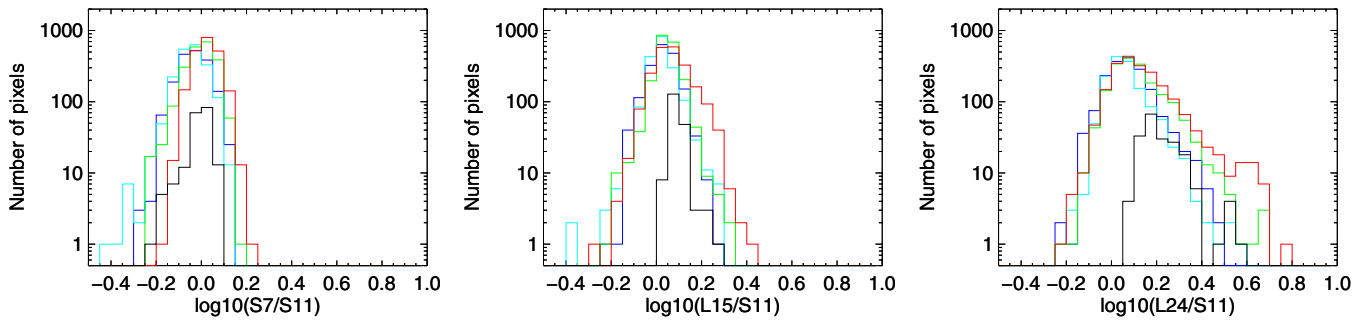(A color version of this figure is available in the online journal.)

Figure 6. Histograms of colors based on S11 for the defined regions with the same color coding as Figure 3.

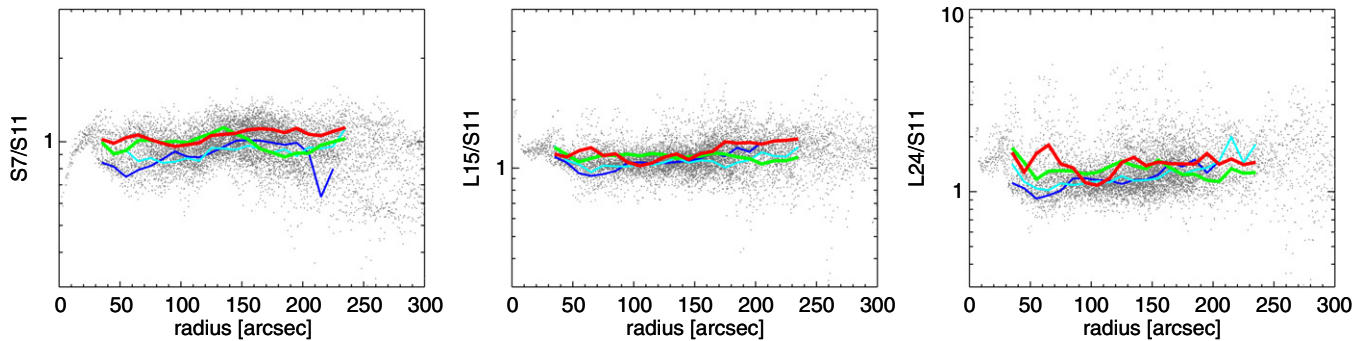(A color version of this figure is available in the online journal.)

Figure 7. Radial profiles of colors based on S11. The azimuthal average every 10″ for each region is overplotted with the same color coding as Figure 3.

(A color version of this figure is available in the online journal.)

SEDs at representative radii and fit a dust model from Draine & Li (2007) to the SED at each radius. For M51a, a radial variation of the PAH fraction and average radiation field is estimated to be small within the disk, while the fraction of the total IR (TIR) luminosity contributed by bright star forming regions decreases with radius. The small radial variation of the former two parameters is consistent with our flat color profiles. On the other hand, L24/S11 is expected to decrease with radius, since the latter parameter is related to the 24 μm/TIR ratio and the 11 μm brightness is thought to correlate with the TIR. This apparent inconsistency indicates that S11 is not a perfect substitution for the TIR. The average and rms of each color have been calculated for each region and are listed in Table 3.

In the following, we discuss colors based on S11 only. For other colors, see the Appendix.

Table 3
Colors Based on S11 for Each Region

Region	S7/S11	L15/S11	L24/S11
Center	0.9 ± 0.1	1.2 ± 0.1	1.7 ± 0.4
Arm 1	1.0 ± 0.1	1.1 ± 0.1	1.3 ± 0.4
Arm 2	1.1 ± 0.1	1.2 ± 0.2	1.4 ± 0.6
Interarm 1	0.9 ± 0.1	1.1 ± 0.1	1.2 ± 0.3
Interarm 2	0.9 ± 0.1	1.1 ± 0.1	1.2 ± 0.3

4.2.1. S7 versus S11

Sakon et al. (2007) presented an *AKARI* S7/S11 map of the nearby spiral galaxy NGC 6946 and found that the ratio is larger than unity in arm regions and less than unity in interarm regions. They interpreted this trend as PAHs being ionized
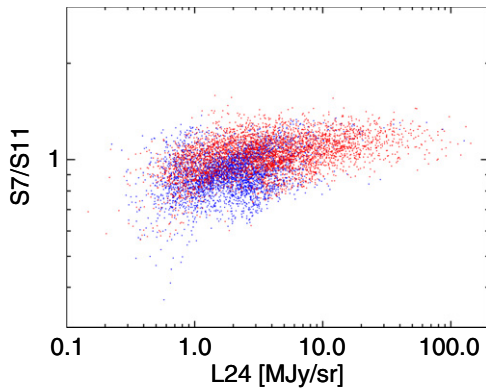
Figure 8. S7/S11 ratio vs. L24 surface brightness. Red is for arm regions while blue is for interarm regions.

(A color version of this figure is available in the online journal.)

around massive star forming regions and the 7.7 μm PAH feature thus becoming brighter. Consistently, the PAH band ratio of 7.7 μm/11.3 μm is found to be larger in arm regions from the *ISO* spectral data (Vogler et al. 2005; Galliano et al. 2008).

From the color maps in Figure 5, we found that S7/S11 traces the global arm structure of M51a, which is consistent with the trend found in NGC 6946. However, the difference in average between arm and interarm regions is only comparable to the rms, as listed in Table 3. Figure 6 also shows that S7/S11 histograms for the arm and interarm regions overlap and that their difference is small compared with their width. We attribute this to two factors: arm width and feathers. First, if arms were defined by eye based on MIR images, they could be narrower than the current definition from the smooth stellar model image. As is obvious from Figure 5, a fraction of arms show S7/S11 < 1. Second, the S7/S11 values in the interarm feathers are similar to the values in the arms. This S7/S11 distribution therefore indicates that the underlying gravitational structure does not completely alter the PAH properties.

To investigate the cause of the S7/S11 variation, we plot the ratio versus L24 surface brightness in Figure 8 with the hypothesis that star forming activity promotes PAH ionization. The correlation is, however, not very tight, and in fact the ratio stays almost flat with respect to the L24 brightness in the arm regions. This plot indicates that the activeness of star formation is not the dominant factor driving the S7/S11 variation. In support of this result, Smith et al. (2007) used *Spitzer*/Infrared Spectrograph (IRS) spectra and found a nearly constant PAH band ratio $L(7.7)/L(11.3)$ across about two orders of magnitude in [Ne III]/[Ne II], an indicator of radiation hardness, for star forming nuclei. Gordon et al. (2008) also showed that the PAH band ratios of H II regions in the nearby galaxy M101 do not depend strongly on the radiation hardness, while the equivalent width of each band feature decreases under very hard radiation.

We also found that in the inner part of Arm 1 the ratio is larger on the downstream side, while this is not true for Arm 2, where most peaks appear around the middle point. This difference indicates that the variation of PAH ionization conditions with respect to the arm structure (i.e., the evolution across the spiral arms) is different between the two arms. Egusa et al. (2009) found that spatial offsets between the arms of molecular gas and H II regions are well explained by the spiral density wave hypothesis (e.g., Lin & Shu 1964) for Arm 1 but not for Arm 2. These differences in properties of the two arms imply that the effect of the tidal interaction with M51b is more significant in

Arm 2. We should, however, note here that the arm properties (and thus their differences) strongly depend on how the arm regions are defined.

As already noted above, no clear radial trend of S7/S11 has been found for the disk (Figure 7). In the central region ($r \leqslant 30''$), the ratio steeply decreases toward the nucleus, which is consistent with *Spitzer*/IRS results such that $L(7.7)/L(11.3)$ is small in the M51a nucleus (Smith et al. 2007). Since the decreasing trend of $L(7.7)/L(11.3)$ with [Ne III]/[Ne II] is found for active nuclei, contrary to a flat distribution for star forming nuclei, smaller or ionized PAHs responsible for the 7 μm feature are thought to be selectively destroyed in the nucleus of M51a.

4.2.2. L15 and L24 versus S11

The spatial distributions of the other colors, i.e., L15/S11 and L24/S11, are more patchy, as shown in Figure 5. A high ratio is found in individual star forming regions, which mostly reside within the arms, while the broad S7/S11 distribution traces the global arm structure.

As is clearly seen in Figure 7 and Table 3, the difference in the average colors between the arm and interarm regions is even less distinct compared with their profile widths. Meanwhile, the histograms in Figure 6 show that larger color values are more frequently seen in the arm regions, especially in the case of L24/S11. These results indicate that the very high ratios in a small number of pixels contribute to the large dispersion but not to the average.

The steep rise toward the center reflects the harsh environments around the active nucleus where the interstellar dust is heated to a very high temperature.

4.3. Color–Color Diagram

In Figure 9, we present color–color diagrams. In the left two panels, data points are color-coded by the defined regions—red for arm, blue for interarm, and black for center. Since the two arm (interarm) regions do not differ significantly as presented above, we do not distinguish them hereafter. While most of the points for the center overlap with the arm points, four points reside in a distinct area that corresponds to the active nucleus.

In the middle two panels, the model calculation from Draine & Li (2007, hereafter DL07) is superimposed on the data points in gray. The color represents the fraction of the total dust mass contributed by PAHs (q_{PAH}), in the sense that it increases from red (0.47%) to blue (4.58%). The range of the other two variable parameters, the minimum threshold for the radiation strength (U_{min}) and the dust mass fraction exposed to $U_{min} < U \leqslant U_{max}$ (γ), was taken to be as wide as available: $\gamma = 0$–1 and $U_{min} = 0.1$–3×10^5. Note that U has units of the local MW radiation field. From these plots, it is clear that the observed color distribution is not fully covered by the combination of parameters employed in DL07. While Draine & Li (2001) presented a strong dependence of the band ratio 11.3 μm/7.7 μm on the ionization state, DL07 adopted a typical PAH ionization fraction for the solar neighborhood ISM as a function of grain size. As a consequence, the profile of PAH band emission from the DL07 models does not vary a lot according to environment except in very strong radiation fields (see their Figure 13), resulting in the very narrow range in predicted S7/S11 ratios.

Given the importance of variation of the PAH ionization state, as discussed above, we decided to construct a new simple model constituting neutral and ionized PAHs and larger dust grains with their relative abundance as an independent variable. Since we
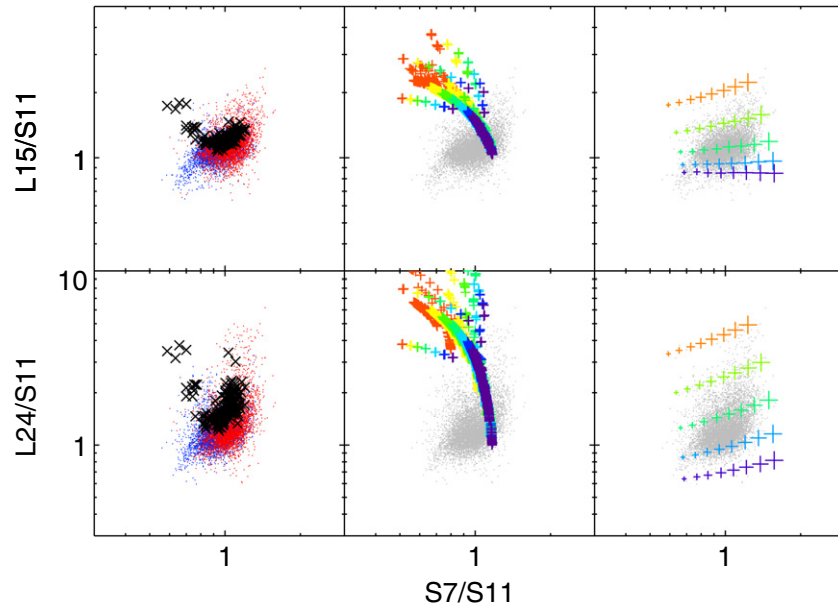
Figure 9. Left: color–color diagrams of observational data color-coded by the defined regions. Blue and red dots represent interarm and arm regions, respectively, while black x symbols are for the center. Middle: the model predictions from DL07 indicated by crosses, color-coded by the PAH fraction q_{PAH}. The color changes from red to blue as q_{PAH} increases. Right: model predictions from this work indicated by crosses. The symbol size and color represent p_0 and p_1 in Equation (1), respectively.

(A color version of this figure is available in the online journal.)

only have MIR data where the cold dust contribution is small, we use a modified blackbody spectrum with a single temperature $T = 100$ K to represent the flux from larger dust grains and call it a WD component. The total emission from these three components are given by

$$(1 - p_0) \times I_\nu(\text{PAH0}) + p_0 \times I_\nu(\text{PAH1}) + p_1 \times \kappa B_\nu(T = 100 \text{ K}),$$
(1)

where $I_\nu(\text{PAH0})$ and $I_\nu(\text{PAH1})$ are the intensity for the neutral and ionized PAHs from DL07, respectively, provided by the DustEM code (Compiègne et al. 2011), κ is the dust emissivity function, and B_ν is the Planck function. Each of the three dust components is shown in Figure 1.

We calculate the in-band flux of these dust components by convolving these spectra with the filter response curves of the *AKARI* MIR bands, which are also presented in Figure 1. By varying the two free parameters, p_0 and p_1, i.e., the fraction of ionized PAHs and the WD component, the predicted colors from our model are plotted in the right panels of Figure 9. While the symbol size corresponds to p_0, the symbol color represents p_1, changing from blue to red as it increases. Overall, the WD fraction and the ionized PAH fraction are positively correlated, which indicates that when dust grains are warmer more PAHs are ionized. This trend is consistent with the result of Mori et al. (2012), who presented a positive correlation between the temperature of the heating source and the ionization fraction of PAHs for selected positions in the Large Magellanic Cloud.

The S7/S11 distribution is now well explained by the variation of p_0 from 0% to 70%. The symbols in Figure 9 are plotted every 10%. The other parameter, p_1, is related to $1/q_{PAH}$ in the sense that L15/S11 and L24/S11 increase as they increase. However, note that they are not exactly the same, since p_1 is the ratio of the WD components to PAHs while q_{PAH} is the mass ratio of PAHs to the total dust, including colder components. By adopting the absorption opacity $\kappa = 2.92 \times 10^5 (\lambda/\mu\text{m})^{-2}$ [cm^{2}g^{-1}] from Li & Draine (2001), the dynamic

range of p_1 corresponds to $M_{\text{WD}}/M_{\text{PAH}} = (0.83\text{–}13) \times 10^{-5}$. The symbols in Figure 9 are plotted by changing this parameter by a factor of two.

5. DISCUSSION

Based on the results presented above, we discuss the properties of interstellar dust in the disk of M51a.

5.1. PAH Ionization

From the S7/S11 distribution map (Figure 5), we find that S7/S11 generally traces the global spiral structure of M51a. Although its difference between the arm and interarm regions is only comparable to the rms of their distribution, its variation cannot be reproduced by the dust model parameters provided by DL07 (Figure 9). We attribute this discrepancy to the variation of PAH ionization state, which is not fully implemented in the DL07 model. Our PAH+WD model suggests a significant variation of the ionized PAH fraction (0–70%) within the disk of M51a.

The balance of ionization and recombination of PAHs is controlled by $G_0\sqrt{T_{\text{gas}}}/n_e$, where G_0 is the radiation field strength, n_e is the electron density, and T_{gas} is the gas temperature (e.g., Tielens 2008). However, these parameters have been determined only in a few Galactic regions, so their correlation with the relative strength of PAH features is investigated only indirectly for extragalactic sources (Galliano et al. 2008). Since all of these three parameters are supposed to become larger in active regions such as galactic nuclei and H II regions, PAH ionization is expected to proceed in arm regions, where star formation is more active than in interarm regions.

Other candidates besides PAH ionization for changing the PAH band ratio or the S7/S11 color are the PAH size distribution and the shape of the radiation field spectra, both of which are investigated by Galliano et al. (2008) and Draine (2011). For the

former, S7/S11 should become smaller when small-size PAHs are less abundant. One indicator for the size distribution of PAHs is the ratio of the 6.2 μm and 7.7 μm band features. Galliano et al. (2008) found that this ratio was relatively constant in star forming galaxies, which suggests that the size distribution does not significantly vary under the conditions of normal star formation. It is thus unlikely that the PAH size distribution is responsible for the difference in S7/S11 between the arm and interarm regions. For the latter, S7/S11 should become larger when the radiation is harder. Although the enhancement of the PAH 7.7 μm/11.3 μm ratio due to radiation from young stars is consistent with the large S7/S11 values in the spiral arms, its effect compared with the normal radiation field is estimated to range from a few to a few tens of percent, which is not enough to explain the observed variations (Galliano et al. 2008; Draine 2011).

As already discussed in Section 4.2.1, neither the gravitational potential nor the star formation rate can solely explain the S7/S11 variation. We therefore conclude that the observed variation in S7/S11 is mainly due to different ionization conditions of PAHs, although the physical conditions triggering their difference is unclear.

5.2. S11 Excess?

From the comparison with the observational data and the DL07 models (middle panels of Figure 9), we find that observational data points with L15/S11 < 1 and L24/S11 < 1 do exist while the models only predict ratios larger than 1. In the following, we consider the contribution to the S11 flux from components other than interstellar dust, which could result in this discrepancy.

Since the contribution from the stellar continuum has already been subtracted in Section 3.1, another candidate is gas emission lines. Dale et al. (2009) obtained MIR spectra from *Spitzer*/IRS toward selected positions in M51 (mostly star forming regions and nuclei) and measured the strength of these lines. Within the S11 spectral coverage, [Ne II] at $\lambda = 12.81 \mu$m is the strongest line but its contribution to the S11 flux is estimated to be 3% at most. In addition, L15/S11 < 1 and L24/S11 < 1 are mostly found in interarm regions (blue points in the left panels of Figure 9), where emission lines are expected to be weaker.

Therefore, we conclude that the discrepancy between the observations and the DL07 model still remains unaccounted for.

5.3. PAH Fraction

As discussed above, we find an excess in S11 flux compared with the DL07 models. This excess may indicate that the PAH fraction (q_{PAH}) in M51a is larger than 4.58%, which is the largest value employed in the DL07 model. This is an important observational restriction to their model, pointed out for the first time by this work (since their model has mostly been applied to data from *Spitzer*, which does not have a photometric filter at 11 μm.)

Note again that the relative abundance of WD to PAHs employed in our model (p_1) does not perfectly correspond to the PAH fraction discussed here. In order to discuss the fraction of each component including colder dust and its spatial variation, data at longer wavelengths (i.e., FIR and mm) with a high spatial resolution are needed; determining q_{PAH} is beyond the scope of this paper.

5.4. Very Small Grains?

In the right panels of Figure 9, we plot the predicted colors from the PAH+WD model over the observed colors. While the two parameters are chosen to cover the observed distribution of L24/S11 versus S7/S11 (the bottom right panel), the L15/S11 distribution (the top right panel) is also covered with the same parameter range. This result indicates that one $T = 100$ K component is enough to explain the *AKARI* MIR colors and that hotter dust components such as very small grains (VSGs) stochastically heated to a very high temperature are not required. On the other hand, Smith et al. (2007) employed multiple dust temperature components to fit the observed IR spectra of nearby star forming galaxies. This apparent inconsistency might be due to differences in observing methods (imaging and spectroscopy) and the wavelength coverage. However, we should note that our result does not fully reject multiple temperature components and the presence of VSGs.

5.5. Extinction Effects

We estimate here the effects from dust extinction on the observed band fluxes, which have been neglected so far. Foreground extinction is estimated from the Galactic dust distribution (Schlegel et al. 1998). At the position of M51a, $A_V = 0.115$ mag. Extinction from dust within the galaxy is more difficult to derive. Calzetti et al. (2005) measured the amount of extinction toward H II regions in M51a with a 13″ aperture and obtained a median value of $A_V \simeq 2.6$ mag for $r \simeq 8''$–80″. While Prescott et al. (2007) found that the extinction in Hα decreases by 0.9 magnitudes over the optical radius of M51, Boissier et al. (2007) and Muñoz-Mateos et al. (2009) found similar gradients for the extinction in the UV. These radial gradients indicate even smaller extinction in the outer disk.

From models provided by Draine (2003), $A(\lambda)/A_V \sim$ 0.01–0.05 for the four representative wavelengths of the MIR bands. We thus estimate that the in-band flux is underestimated by ∼3%–13% due to extinction. We should note here that the extinction effect cannot explain the S11 excess, since it is largest in S11 due to the silicate absorption feature and the extinction correction would increase the S11 excess even more. Furthermore, the excess is mostly observed in the interarm regions where the extinction is plausibly less than in the other regions.

6. SUMMARY

We present four MIR band images of the nearby pair of galaxies M51 taken under two pointed observations with the IRC onboard *AKARI*. The FoV of the IRC is about 10′, covering almost the entire M51 system. Additional reduction procedures besides the standard pipeline are also summarized, which are fully described in F. Egusa et al. (2013, in preparation). The angular resolution is set to be 7″4 (∼300 pc) in FWHM after the PSF correction.

A contribution from the stellar continuum to each *AKARI* MIR band is estimated from the models of Mentuch Cooper et al. (2012) and subtracted from the observed image to obtain a dust only image. Following Dumas et al. (2011), we apply wavelet analysis to the stellar model image and define arm and interarm regions in the disk of the main spiral galaxy M51a.

The arm/interarm contrast is found to be slightly different between the four MIR bands. The lowest contrast for S11 is interpreted to mean that among the four *AKARI* MIR bands, this band best represents the total dust distribution including colder
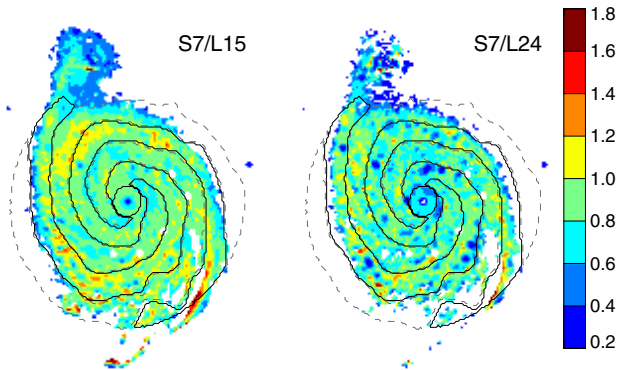
Figure 10. Same as Figure 5 but for S7/L15 and S7/L24.

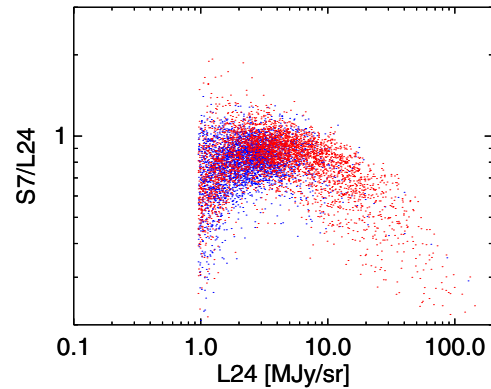(A color version of this figure is available in the online journal.)

Figure 11. S7/L24 vs. L24 surface brightness. The red and blue points represent the arm and interarm regions, respectively. The cutoff at the faint end corresponds to the 5σ threshold applied when calculating S7/L24.

(A color version of this figure is available in the online journal.)

components. Meanwhile, the contrast is highest for L24, which traces warmer dust heated from star forming activity.

The flux ratio between the bands, i.e., color, has been measured over the disk of M51a. As already found in another spiral galaxy (NGC 6946) by Sakon et al. (2007), S7/S11 traces the global spiral arm pattern well with higher values in the arms. However, its difference between the arm and interarm regions is found to be only comparable to the rms in the distributions. Furthermore, S7/S11 does not tightly correlate with the L24 brightness, an indicator of star formation. These results indicate that a variation of S7/S11 does exist but that the underlying stellar potential and the activity of star formation are not dominant controlling factors.

A comparison with dust models by DL07 also suggests that the variation of PAH ionization states needs to be taken into account. Employing a new model, which comprises ionized and neutral PAHs and $T = 100$ K dust grains with their relative abundances being variable, we successfully cover the observed distribution in the color–color plots. The observed S7/S11 variation is explained by changing the ionized PAH fraction from 0% to 70%. The fraction of ionized PAHs and WD is positively correlated in the disk of M51a, indicating that when dust grains are warmer more PAHs are ionized. By comparing the observed colors and the models of DL07 (2007), we also find an excess in the S11 surface brightness, which cannot be explained by stellar continuum, gas emission lines, or extinction effects. This excess indicates that the PAH contribution to the total interstellar dust mass is likely higher than previous estimates in M51a.

We emphasize that data at 11 μm are essential for the above discussions and for investigating PAH properties.

APPENDIX

COMPARISON OF COLORS WITH LITERATURE VALUES

Here, we present the distribution of colors not based on S11 and compare the *AKARI* results with previous studies. As well as the colors discussed in Section 4.2, a 5σ threshold has been employed when calculating colors.

A.1. S7 versus L15

Sauvage et al. (1996) analyzed LW2 (7 μm) and LW3 (15 μm) images of M51 from *ISO* and found that LW2/LW3 becomes small in the arm regions. They interpreted this result as a large dependence of LW3 flux on temperature; away from an arm, the temperature decreases, resulting in high LW2/LW3 ratios in the interarm regions.

In contrast with the S7/S11 map, the *AKARI* S7/L15 map shown in Figure 10 is complicated. At positions where Sauvage et al. (1996) derived the LW2/LW3 ratio, the S7/L15 ratio is slightly lower in the arm compared with the adjacent interarm region. The trend, however, does not seem to be universal. On average, we do not find any systematic difference in S7/L15 for the arm and interarm regions.

Roussel et al. (2001) measured LW3/LW2 for selected bright objects in M51, mostly star forming regions and the companion, and showed that the ratio is almost constant around 1.0–1.5 with no significant radial trend. A roughly constant LW2/LW3 color was also found in the disk of NGC 6946 (Helou et al. 1996). Consistently, we confirm that S7/L15 values for both the arm and interarm regions do not show any radial dependence, while they steeply decrease toward the nucleus in the center region.

A.2. S7 versus L24

Bright PAH band features around 7 μm and continuum emission around 24 μm are often regarded as star formation indicators. However, their spatial distributions around H II regions have been found to differ. By subtracting the stellar contribution from *Spitzer* IRAC4 (8 μm) images and comparing them with MIPS24 (24 μm) images, many authors have reported that the stellar subtracted IRAC4, which is dominated by PAH features, is bright around the border of H II regions, while MIPS24 images peak at their center (e.g., Helou et al. 2004; Bendo et al. 2006). The wavelet analysis by Dumas et al. (2011) also supports this finding in the sense that the amplitude shows

a peak around a 10″ scale for MIPS24 data while it is flat around that scale for stellar subtracted IRAC4 data. From these results, PAH grains are thought to be destroyed in the centers of H II regions, where the stellar radiation is hard and strong.

We also find a consistent trend in our *AKARI* S7/L24 map (Figure 10), in which the ratio is small in bright H II regions in spiral arms. In order to investigate the relationship with the star formation rate, S7/L24 is plotted against L24 surface brightness in Figure 11. At the bright end, i.e., around H II regions, the ratio decreases with increasing L24, which is consistent with the above picture. At the faint end, on the other hand, it stays mostly flat or even increases with L24, though the scatter is large. We deduce that this bimodal relationship reflects multiple origins of the L24 flux; while young massive stars are the dominant source for bright objects, old and less massive stars contribute significantly where massive star formation is absent. The turning point of these two trends is L24 $\sim$3–5 MJy sr^{-1}, which is around the mode of the L24 surface brightness distribution for both the arm and interarm regions (Figure 4).

We again do not find any systematic difference in average S7/L24 between the arm and interarm regions. A radial dependence is also absent except in the central region, where it steeply decreases toward the nucleus.

REFERENCES

Allamandola, L. J., Tielens, A. G. G. M., & Barker, J. R. 1989, ApJS, 71, 733
Arimatsu, K., Onaka, T., Sakon, I., et al. 2011, PASP, 123, 981
Bendo, G. J., Dale, D. A., Draine, B. T., et al. 2006, ApJ, 652, 283
Boissier, S., Gil de Paz, A., Boselli, A., et al. 2007, ApJS, 173, 524
Calzetti, D., Kennicutt, R. C., Jr, Bianchi, L., et al. 2005, ApJ, 633, 871
Calzetti, D., Kennicutt, R. C., Engelbracht, C. W., et al. 2007, ApJ, 666, 870
Compiègne, M., Verstraete, L., Jones, A., et al. 2011, A&A, 525, A103
Daigle, O., Carignan, C., Amram, P., et al. 2006, MNRAS, 367, 469
Dale, D. A., Smith, J. D. T., Schlawin, E. A., et al. 2009, ApJ, 693, 1821
Draine, B. T. 2003, ARA&A, 41, 241
Draine, B. T. 2007, ApJ, 657, 810
Draine, B. T. 2011, in PAHs and the Universe: A Symposium to Celebrate the 25th Anniversary of the PAH Hypothesis, EAS Publications Series, Vol. 46, ed. C. Joblin & A. G. G. M. Tielens (Les Ulis, France: EDP Sciences), 29
Draine, B. T., & Li, A. 2001, ApJ, 551, 807
Dumas, G., Schinnerer, E., Tabatabaei, F. S., et al. 2011, AJ, 141, 41
Egusa, F., Koda, J., & Scoville, N. 2011, ApJ, 726, 85
Egusa, F., Kohno, K., Sofue, Y., Nakanishi, H., & Komugi, S. 2009, ApJ, 697, 1870
Feldmeier, J. J., Ciardullo, R., & Jacoby, G. H. 1997, ApJ, 479, 231
Fioc, M., & Rocca-Volmerange, B. 1997, A&A, 326, 950
Galliano, F., Madden, S. C., Tielens, A. G. G. M., Peeters, E., & Jones, A. P. 2008, ApJ, 679, 310
Gordon, K. D., Engelbracht, C. W., Rieke, G. H., et al. 2008, ApJ, 682, 336
Helou, G., Malhotra, S., Beichman, C. A., et al. 1996, A&A, 315, L157
Helou, G., Roussel, H., Appleton, P., et al. 2004, ApJS, 154, 253
Högbom, J. A. 1974, A&AS, 15, 417
Kaneda, H., Onaka, T., Kitayama, T., Okada, Y., & Sakon, I. 2007, PASJ, 59, 107
Kaneda, H., Onaka, T., Suzuki, T., Takahashi, H., & Yamagishi, M. 2009, in ASP Conf. Ser. 418, AKARI, a Light to Illuminate the Misty Universe, ed. T. Onaka, G. J. White, T. Nakagawa, & I. Yamamura (San Francisco, CA: ASP), 197
Koda, J., Scoville, N., Sawada, T., et al. 2009, ApJL, 700, L132
Lee, J. H., Hwang, N., & Lee, M. G. 2011, ApJ, 735, 75
Leger, A., & Puget, J. L. 1984, A&A, 137, L5
Li, A., & Draine, B. T. 2001, ApJ, 554, 778
Lin, C. C., & Shu, F. H. 1964, ApJ, 140, 646
Mentuch Cooper, E., Wilson, C. D., Foyle, K., et al. 2012, ApJ, 755, 165
Mori, T. I., Sakon, I., Onaka, T., et al. 2012, ApJ, 744, 68
Muñoz-Mateos, J. C., Gil de Paz, A., Boissier, S., et al. 2009, ApJ, 701, 1965
Murakami, H., Baba, H., Barthel, P., et al. 2007, PASJ, 59, 369
Onaka, T., Matsuhara, H., Wada, T., et al. 2007b, PASJ, 59, 401
Onaka, T., Tokura, D., Sakon, I., et al. 2007a, ApJ, 654, 844
Prescott, M. K. M., Kennicutt, R. C., Jr, Bendo, G. J., et al. 2007, ApJ, 668, 182
Roussel, H., Vigroux, L., Bosma, A., et al. 2001, A&A, 369, 473
Sakon, I., Onaka, T., Wada, T., et al. 2007, PASJ, 59, 483
Sánchez-Gil, M. C., Jones, D. H., Pérez, E., et al. 2011, MNRAS, 415, 753
Sauvage, M., Blommaert, J., Boulanger, F., et al. 1996, A&A, 315, L89
Schlegel, D. J., Finkbeiner, D. P., & Davis, M. 1998, ApJ, 500, 525
Sellgren, K. 1984, ApJ, 277, 623
Shetty, R., Vogel, S. N., Ostriker, E. C., & Teuben, P. J. 2007, ApJ, 665, 1138
Smith, J. D. T., Draine, B. T., Dale, D. A., et al. 2007, ApJ, 656, 770
Tanabé, T., Sakon, I., Cohen, M., et al. 2008, PASJ, 60, 375
Tielens, A. G. G. M. 2008, ARA&A, 46, 289
Turner, J. L., & Ho, P. T. P. 1994, ApJ, 421, 122
Vogler, A., Madden, S. C., Beck, R., et al. 2005, A&A, 441, 491